

JGR Solid Earth

RESEARCH ARTICLE

10.1029/2024JB028900

Imaging the Garlock Fault Zone With a Fiber: A Limited Damage Zone and Hidden Bimaterial Contrast

James Atterholt¹ , Zhongwen Zhan¹ , Yan Yang¹ , and Weiqiang Zhu^{1,2}

¹Seismological Laboratory, California Institute of Technology, Pasadena, CA, USA, ²Department of Earth and Planetary Science, University of California Berkeley, Berkeley, CA, USA

Key Points:

- We use a distributed acoustic sensing array that crosses the Garlock Fault to investigate its structure
- We find that the low velocity zone around the fault is mostly shallow, suggesting the damage zone at depth is at most narrow
- We find a clear bimaterial contrast at depth, which was hidden by the shallow crust, that suggests a preferred westward directivity

Supporting Information:

Supporting Information may be found in the online version of this article.

Correspondence to:

J. Atterholt,
atterholt@caltech.edu

Citation:

Atterholt, J., Zhan, Z., Yang, Y., & Zhu, W. (2024). Imaging the Garlock Fault Zone with a fiber: A limited damage zone and hidden bimaterial contrast. *Journal of Geophysical Research: Solid Earth*, 129, e2024JB028900. <https://doi.org/10.1029/2024JB028900>

Received 14 FEB 2024

Accepted 12 JUL 2024

Author Contributions:

Conceptualization: James Atterholt, Zhongwen Zhan

Data curation: James Atterholt, Zhongwen Zhan

Formal analysis: James Atterholt

Funding acquisition: James Atterholt, Zhongwen Zhan

Investigation: James Atterholt

Methodology: James Atterholt, Zhongwen Zhan, Yan Yang, Weiqiang Zhu

Resources: Zhongwen Zhan

Software: James Atterholt, Yan Yang, Weiqiang Zhu

Supervision: Zhongwen Zhan

Validation: James Atterholt

Visualization: James Atterholt

Writing – original draft: James Atterholt

Writing – review & editing: James Atterholt, Zhongwen Zhan, Yan Yang

Abstract The structure of fault zones and the ruptures they host are inextricably linked. Fault zones are narrow, which has made imaging their structure at seismogenic depths a persistent problem. Fiber-optic seismology allows for low-maintenance, long-term deployments of dense seismic arrays, which present new opportunities to address this problem. We use a fiber array that crosses the Garlock Fault to explore its structure. With a multifaceted imaging approach, we peel back the shallow structure around the fault to see how the fault changes with depth in the crust. We first generate a shallow velocity model across the fault with a joint inversion of active source and ambient noise data. Subsequently, we investigate the fault at deeper depths using travel-time observations from local earthquakes. By comparing the shallow velocity model and the earthquake travel-time observations, we find that the fault's low-velocity zone below the top few hundred meters is at most unexpectedly narrow, potentially indicating fault zone healing. Using differential travel-time measurements from earthquake pairs, we resolve a sharp bimaterial contrast at depth that suggests preferred westward rupture directivity.

Plain Language Summary Fault zone structure is important because it influences the physics of earthquake ruptures. Imaging fault zones at depth, where large earthquakes typically happen, is challenging because fault zones are narrow and seismic imaging resolution degrades with depth. Dense seismic arrays deployed across faults can help resolve important properties of fault zones at depth. Fiber optic seismology allows for the deployment of dense arrays across faults for long periods of time with low logistical burden. We use a fiber optic array that crosses the Garlock Fault to explore important characteristics of the fault zone at different depths. We find that there is no extensive low velocity feature at depth, potentially suggesting healing of the fault damage zone. Additionally, when we remove the contribution of the complicated velocity structure of the shallow crust, we recover a sharp velocity contrast across the fault which may have implications for the propagation behavior of future ruptures.

1. Introduction

Fault zone structure plays an important role in the behavior of earthquake ruptures. Damage in the immediate vicinity of the fault alters the permeability and rheology of fault-adjacent rocks, potentially affecting the movement of fluids near the fault (Caine et al., 1996) and changing the dynamic properties of ruptures (Dunham et al., 2011; Thakur et al., 2020). Observational work has shown that large ruptures often propagate unilaterally (e.g., Atterholt & Ross, 2023; J. J. McGuire et al., 2002); simulations and experimental work suggest that a bimaterial contrast across the fault at seismogenic depths promotes asymmetric ruptures, but the consequences for future directivity of faults is unclear (Andrews & Ben-Zion, 1997; Anooshehpour & Brune, 1999; Cochard & Rice, 2000; Harris & Day, 2005; Huang, 2018; Ranjith & Rice, 2001; Xia et al., 2005). Recent simulations suggest that, for sequences of earthquakes, bimaterial contrasts bias the nucleation sites toward asymmetric ruptures and a preferred rupture direction (Abdelmeguid & Elbanna, 2022; Erickson & Day, 2016). This consequent directivity can amplify ground motion in the path of the propagating rupture, which is an important consideration when evaluating rupture hazards and dynamic stress changes.

The Garlock Fault is a major left-lateral strike-slip fault that extends from the San Andreas to the southern tip of Death Valley and bisects the Eastern California Shear Zone. This fault has been quiet during the historical period but is known to have hosted several large earthquakes in the past few thousand years (Dawson et al., 2003; Madden Madugo et al., 2012; McGill & Rockwell, 1998). The most recent known event on the Garlock Fault took place several hundred years ago, and thus the fault is expectedly late in its interseismic period. Results from a

well-studied site on the central segment of the Garlock Fault, which is of particular interest to this study, suggest the most recent earthquake to rupture the surface along the central segment of the fault took place between 1450 and 1610 AD (Dawson et al., 2003). The integrated displacement along the fault is approximately 50 km (Davis & Burchfiel, 1973; Monastero et al., 1997; Smith, 1962) and thus the Garlock is a mature fault with an expectedly well-developed damage zone. Based on empirical scaling relationships between fault displacement and damage zone width, the displacement on the Garlock would suggest a damage zone with a wide range of potential widths, but likely exceeding 100 m (Savage & Brodsky, 2011). Additionally, the large displacement along the fault could have potentially juxtaposed lithologies with distinct seismic velocities, creating a bimaterial contrast across the fault. But the juxtaposition observed at the surface is complicated (see Figure S1 in Supporting Information S1 for geologic map) and is not necessarily representative of the material contrast at depth. Recently, the 2019 Ridgecrest earthquake sequence triggered creep and an earthquake swarm on the Garlock Fault (Ross et al., 2019). A rupture on the Garlock is of concern because of its proximity to several communities and because it would likely impose significant dynamic and static stress changes on the San Andreas (Toda & Stein, 2020) or could potentially be triggered to produce a large aftershock of a rupture on the San Andreas, as in the 2023 Kahramanmaraş earthquake sequence (Jia et al., 2023).

Imaging fault zones is a challenging problem, particularly at depth, because fault zones are narrow structures, and the resolution of imaging techniques, such as travel-time tomography, typically degrade with depth. Fault structure at depth is important because large earthquakes typically nucleate at least several kilometers (~5 km) below the surface (Hauksson et al., 2012), and the fault zone at these depths is thus important for understanding the physics of large ruptures. Hereafter, we refer to depths at which large earthquakes typically nucleate as seismogenic depths. Travel-times from individual earthquakes can sample structure near the fault (Ozakin et al., 2012), but these measurements are depth-integrated, and thus make drawing conclusions about the fault at seismogenic depths difficult. Fault zone trapped waves (e.g., Ben-Zion et al., 2003; Catchings et al., 2016; Qiu et al., 2021) and fault zone head waves (e.g., Allam et al., 2014; McGuire & Ben-Zion, 2005) have been used to image fault damage zones and bimaterial contrasts respectively, with great success. However, a recent study of the Garlock fault (H. Qiu et al., 2023) shows no fault zone trapped wave observations and some weak fault zone head wave observations, which are also depth-integrated, on the Garlock. This would suggest the damage zone is not an efficient trapping structure and that there is a material contrast across the fault; but the finer details and the depth-dependent behavior of these features are ambiguous. Imaging the depth-dependent properties of the fault damage zone and characterizing the properties of the fault interface at seismogenic depths thus present significant challenges.

Distributed acoustic sensing (DAS) is a technique that measures strain in a fiber optic cable using optical interferometry on backscattered light from laser pulses in the fiber. DAS arrays measure strain at high spatial and temporal frequency and can be deployed with minimal effort for long periods of time. In this study, we use a DAS array that crosses the Garlock to image the depth-dependent structure of the fault zone. To accomplish this, we apply a framework that uses multiple methods with complimentary depth sensitivities to recover the depth-dependent structure of the fault zone. This kind of approach has been successfully applied using dense arrays that cross fault zones in the past (Jiang et al., 2021; Zhang et al., 2022). We first resolve a high-resolution image of the shallow structure using a joint data set of active source and ambient noise data. Subsequently, we measure the depth-integrated velocity structure on the fault zone using earthquake travel-times from a cluster of earthquakes near the fault. Using a broader set of earthquakes, we infer deeper fault structure using differential travel-times from earthquakes over a larger geographic area. These analyses are all performed using collocated measurements and each uniquely constrain different depth-dependent features of the fault zone.

2. A Heterogeneous Shallow Subsurface

The shallowest part of the fault zone has been shown to exhibit sharp, low-velocity anomalies that contribute to considerable ground motion amplification during earthquakes and may signify damage that facilitates fluid transport (Share et al., 2020; Y. Wang et al., 2019; Zigone et al., 2019). The high heterogeneity imposed by the shallow subsurface may also significantly affect depth-integrated measurements which are used to infer the properties of fault zones at seismogenic depths. The shallowest fault zone structure is thus a natural starting point when seeking to understand the fault zone's full architecture, because this structure may subsequently be used to correct for its universal contribution to depth-integrated observations.

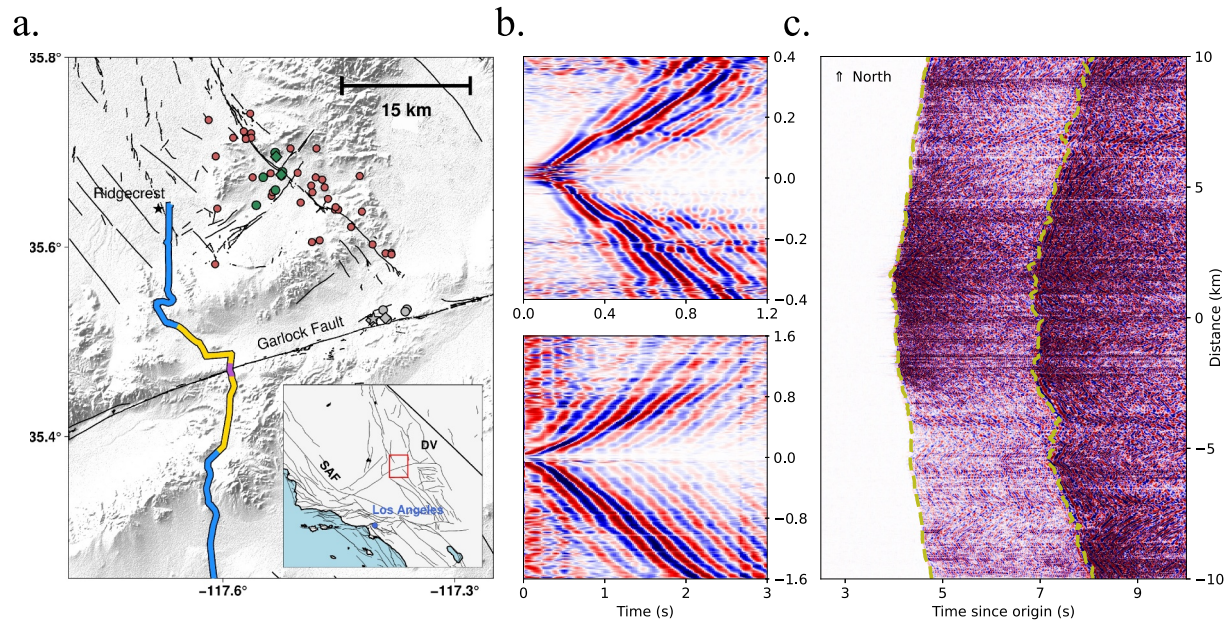


Figure 1. Study setting and data set examples. (a) Map summarizing the data used in this study. Blue, yellow, and purple curves represent the entire DAS array, the segment used for the ambient noise experiment, and the segment used for the active source experiment, respectively. Gray and green points show the earthquakes used to construct the profiles in Figures 2 and 4. The gray star indicates the earthquake shown in (c). The diamond shaped points indicate the earthquakes shown in Figure S8 in Supporting Information S1. Red points show earthquakes that were also used in the inversion for the bimaterial contrast. Locations of the San Andreas Fault (SAF) and Death Valley (DV) are indicated on the inset. (b) Example shot gathers located approximately on the mapped fault trace from the active source (top) and ambient noise experiments (bottom). Active source and ambient noise shot gathers are bandpass filtered between 2–10 and 1–5 Hz respectively. (c) Example of the waveforms from an on-fault earthquake. Olive dotted lines mark the P and S wave picks. Earthquake wavefield is filtered between 1 and 10 Hz. For b and c, zero distance is the location of the intersection between the central strand of the Garlock Fault and the DAS array.

In August of 2021, a DAS array was deployed on a dark fiber traversing a path between Ridgecrest, CA and Barstow, CA. The array spans 100 km with 10-m channel spacing, amounting to 10,000 channels averaging strain over 50 or 100 m, depending on the recording period (see Figure 1). DAS is a powerful tool for characterizing the shallow subsurface (e.g., Atterholt et al., 2022; Cheng et al., 2021; Jousset et al., 2018; Spica et al., 2020; Viens et al., 2022; Yang, Zhan, et al., 2022), and we employ this array to solve for the heterogeneous structure in and around the Garlock Fault. We leverage data with complementary frequency sensitivity from an active source survey that used the in-situ DAS channels as receivers and ambient noise cross-correlations.

The active source experiment was performed using a Propelled Energy Generator (40 kg) source at 10 m intervals along a 1.4 km segment of the array centered on the mapped strand of the Garlock Fault (purple segment; Figure 1a). At each shot location, we performed 10 shots for stacking. During the active source experiment, we reduced the channel spacing and gauge length of the array to 2 and 16 m respectively. To produce virtual shot gathers, we cross-correlate ambient noise for a week of continuous data with 10 m channel spacing and 50 m gauge length. Prior to performing the cross-correlations, we bandpass filter the data between 0.1 and 10 Hz and down-sample the data to 25 Hz. We apply absolute-average temporal normalization and spectral whitening to 1-hr segments of the data and subsequently apply cross-correlation and normalization in the frequency domain (Bensen et al., 2007). We then transform the cross-correlations to the time domain and organize them into common shot gathers for each virtual source. Examples of both active source and virtual source shot gathers are shown in Figure 1b.

To invert for dispersion curves for both sets of shot gathers, we employ a beamforming approach (Yang, Atterholt, et al., 2022). In short, this approach takes a window of stations around each station that recorded an individual shot gather and measures the local phase dispersion. The window used is set according to the approximate wavelength of the data. This technique resolves many dispersion curves at each channel location for each data set. The resultant dispersion curves in the immediate vicinity around the fault are shown in Figure 2, and the dispersion curves for an extended region computed using only the ambient noise data are shown in Figure S2 in Supporting Information S1.

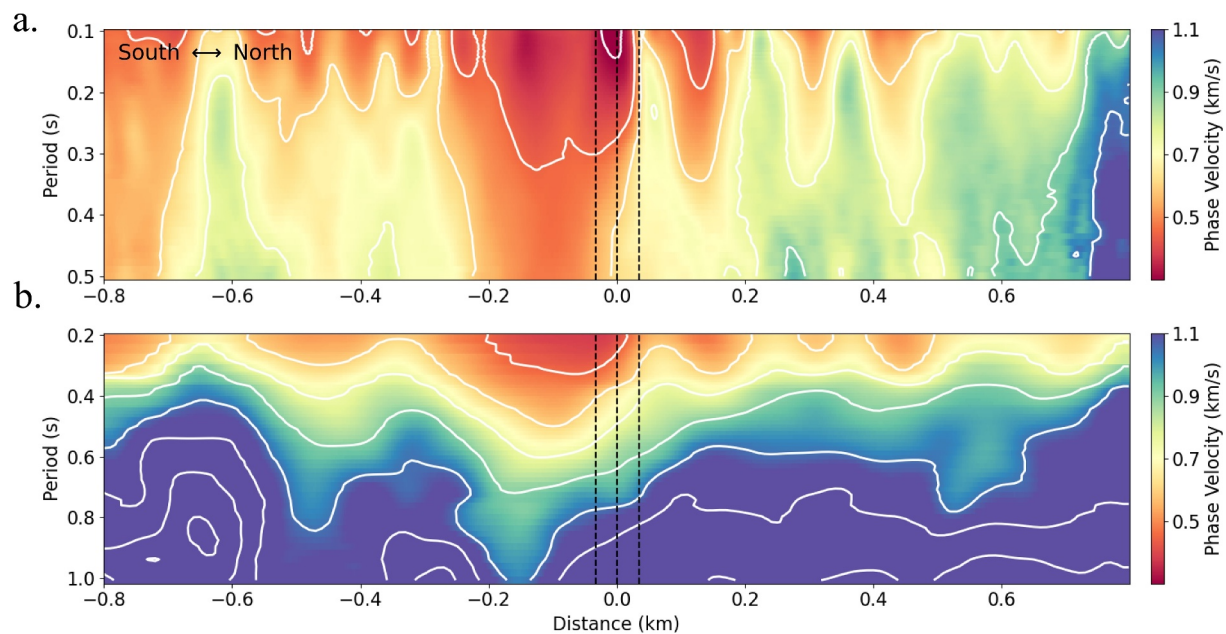


Figure 2. Dispersion curves from the active source experiment (a) and ambient noise cross-correlations (b) along the purple segment of the array in Figure 1. Black dotted lines show locations of mapped strands of the Garlock Fault where they cross the velocity profile.

We subsequently perform a joint inversion to infer the depth-dependent velocity structure around the fault shown in Figure 3. To accomplish this, we use several key components of the level set tomography approach outlined in Muir and Tsai (2020) and Muir et al. (2022). We parameterize our model as a Gaussian random field that is regularized by a Whittle-Matérn covariance function. The covariance function incorporates a dominant length scale, set to 40 m in this study, and a roughness parameter, set to 2.5 in this study. We choose this length scale both because it conservatively exceeds the minimum gauge length and corresponds to the minimum wavelength in our data set. Because of the dominant length scale, some of the high spatial frequency features in the data are not captured in the joint model. This is acceptable for our purposes. Setting the roughness parameter to 2.5 is equivalent to enforcing that each individual realization of the Gaussian random process is twice continuously differentiable. The inversion is solved using the Ensemble Kalman Sampler (Garbuno-Inigo et al., 2020). This solver initializes a set of particles and uses Langevin diffusion dynamics to iterate toward the posterior distribution. We incorporate both sets of data into this inversion by computing the model-data misfit for each data set, weighted by the corresponding standard deviations, at each iteration. For the joint inversion, we up-sample the ambient noise dispersion curve profile so that the dimensions of the two data sets are the same.

We separately perform an inversion using only ambient noise cross-correlation data for an extended portion of the array using the dispersion curves in Figure S2 in Supporting Information S1. Because of the lower spatial resolution of the ambient noise cross-correlation data set, we use a dominant length scale of 200 m for this inversion. We merge this model with our higher resolution near-fault model; the discontinuity between these two models is removed by gradual averaging at the boundaries. The resultant extended model is plotted in Figure S2 in Supporting Information S1. We directly compare the near-fault velocity structure recovered using only the ambient noise data with the model recovered using the joint inversion in Figure S3 in Supporting Information S1. While these two models both recover the first-order low velocity feature near the fault, the joint model recovers a more detailed picture of the fault zone. The higher frequency phase velocity measurements from the active source experiment prevent the underestimation of velocities in the shallowest portion of the model, and the higher spatial frequency of the active source data uncovers the low wavelength variability near the fault trace.

The velocity model in Figure 3 shows a rapid transition from lower-velocity material to higher-velocity material with depth. The heterogeneous lateral structure is responsible for sharp velocity perturbations at and across the fault. There is a clear, low-velocity feature biased toward the south side of the fault with a width of approximately 300 m. This feature could be interpreted as the fault damage zone, but at this depth resolution, it could also be a shallow, potentially fault-associated, basin structure, as has been observed elsewhere (Song & Yang, 2022).

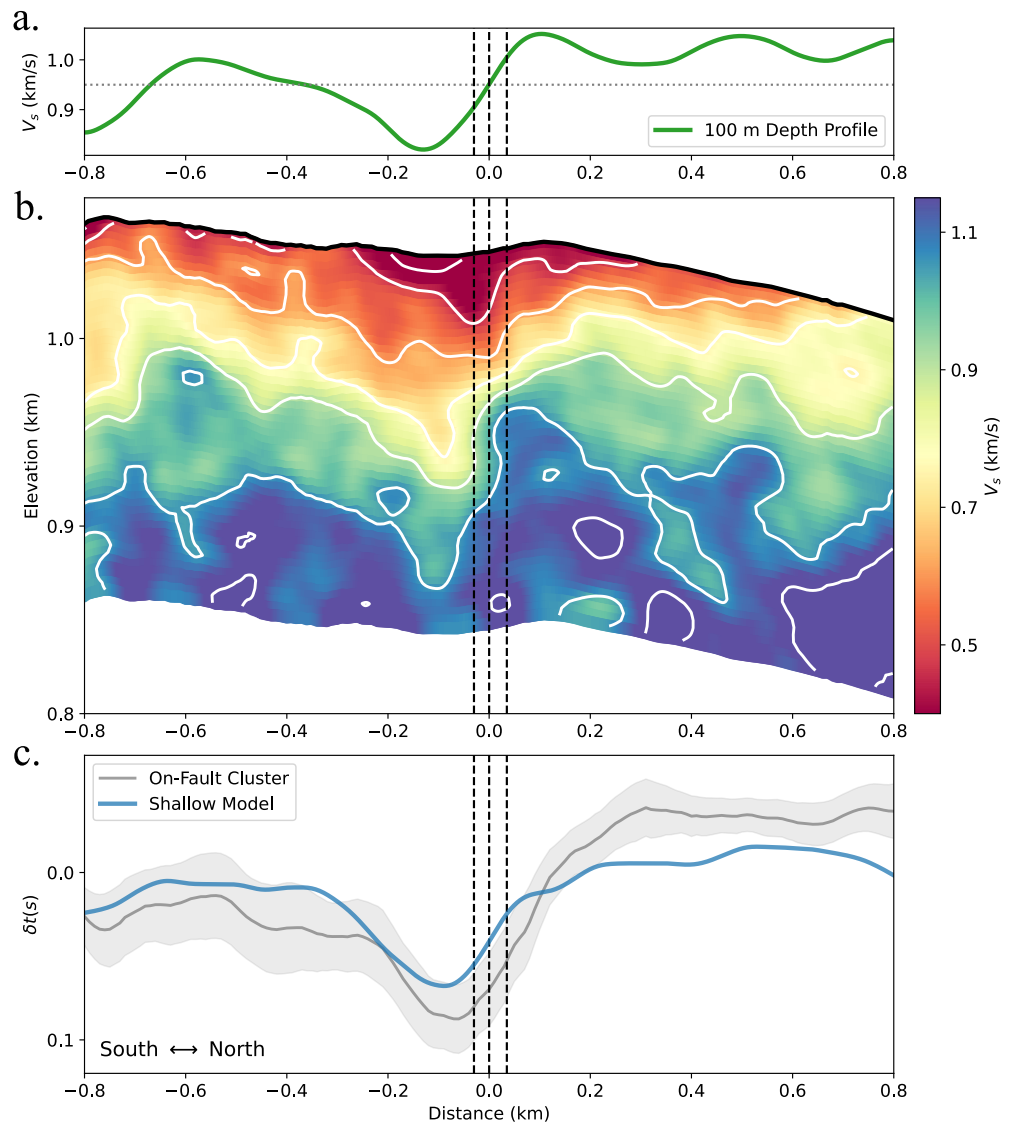


Figure 3. Shallow shear wave velocity model and corresponding model-travel-time perturbation comparison along the purple segment of the array shown in Figure 1. (a) Profile taken from the shallow velocity model around 100 m depth (averaged from 80 to 120 m and smoothed over 200 m laterally) that clearly shows the discontinuity across the fault. (b) Shear wave velocity model from the joint inversion of the active source and ambient noise data. Black dotted lines mark the locations of the array-crossing mapped traces of the Garlock Fault. (c) Travel-time perturbations from the cluster of earthquakes on the fault in Figure 1 and the expected perturbations from the shallow model. Shallow model perturbations are modified by applying a moving average filter corresponding to the gauge length of the fiber recording the earthquake for comparability.

Additionally, low velocities (less than 800 m/s) persist in the top 100 m to the edges of our joint model. To determine if this is potentially a wider compliant zone associated with fault deformation, we can look at the extended model produced using ambient noise cross-correlation in Figure S2 in Supporting Information S1. This model suggests that these low velocities extend at similar depths several kilometers from the fault trace. We thus expect that these low velocities are associated with shallow sediment rather than deformation due to the fault zone. There is also a clear step in velocity across the fault, suggesting a sharp discontinuity due to displacement. The lateral heterogeneity at these depths suggests that the near-fault structure is highly varied, and because local structure plays a large role in ground motion amplification (Aki, 1993), these observations are important for assessing potential ground motion variability due to strong velocity perturbations near faults. Beyond these observations, this model is also a valuable correction term for isolating the fault structure at depth.

3. An Upper Limit on Damage Zone Size

Earthquake travel-time measurements are sensitive to the velocity structure along the entire ray path, including both seismogenic depths and the shallow crust. Due to the highly productive 2019 Ridgecrest earthquake aftershock sequence, the area around the Garlock fault has produced many earthquakes with variable depths to the northeast of the array (Ross et al., 2019). We first focus on a cluster of earthquakes near the Garlock Fault approximately 20 km east of the array and 9 km deep (Figure 1). We use a deep learning algorithm, PhasenetDAS (Zhu et al., 2023), which is designed specifically for DAS data, to pick shear wave phase arrivals from these earthquakes. In short, PhasenetDAS generates training data sets by generating noisy labels for DAS data using Phasenet (Zhu & Beroza, 2018) and refining the labels using GaMMA (Zhu et al., 2022), a phase association algorithm. PhasenetDAS was partially trained using this data set and, by visual inspection, performs very well for the events used in this study. Examples of these picks are shown in Figure 1 and Figure S8 in Supporting Information S1. To compute the travel-time perturbations for each event, we compute the expected travel-times for a 1D model and subtract these from the observed travel-times. We modify a local 1D velocity profile from the SCEC Community Velocity Model (CVMS) (E. Lee et al., 2014) and compute the travel-times using TauP (Crotwell et al., 1999). The velocity profile used, and the approximate depth-sensitivity of the ray paths are shown in Figure S4 in Supporting Information S1. We then perform an elevation correction assuming an S-wave velocity from the top layer of the Hadley-Kanamori model (Hadley & Kanamori, 1977). The average travel-time perturbations for all events in the cluster are shown in Figure 3.

We can compute the expected travel-time perturbations for the near-surface structure by computing the travel-time differences for a wavefront propagating through our shallow subsurface velocity model. As shown in Figure 3, the travel-time perturbations very close to the fault are highly consistent between those measured from the earthquakes and the expected perturbations from our shallow velocity model. This would suggest that most of the depth integrated structural contributions near the fault are coming from top few hundred meters, and thus the structural variability at depth, including the variability resulting from the fault damage zone, is minor.

The earthquake travel-times are measured using waveform data with a power spectrum maximum at 6.5 Hz and substantial energy at 10 Hz, as shown in Figure S5 in Supporting Information S1. Assuming shear wave velocities directly below our shallow velocity model are slightly higher than 1 km/s, as we observe at the base of our shallow velocity model, we may expect the wavelengths that control the sensitivity of our measurements to be between 100 and 200 m and potentially as large as 300 m. We can use these wavelength estimates to better understand the sensitivity of our measurements to low velocity zone parameters at depths below 200 m. With this purpose, we perform an evaluation of travel-time perturbations due to different fault zone parameterizations using an Eikonal equation solver (Sethian, 1996; White et al., 2020), and we apply different moving average filters to approximate sensitivities at wavelengths of 100, 200, and 300 m. The results of these computations, shown in Figure S6 in Supporting Information S1, suggest our measurements are sensitive to low velocity zone features deeper than our velocity model with widths of at least 150 m, and potentially as narrow as 100 m, and velocity perturbation amplitudes above 5%. This would suggest that there is a rapid narrowing or decay of the low velocity zone below 200 m depth, implying that the Garlock fault's damage zone does not host a wide or high amplitude low velocity feature at depth. The observed low-velocity feature is very small compared to some other faults, such as the Calico Fault, another major Southern California Fault late in its interseismic period, which hosts a substantial low-velocity feature (Figure S6 in Supporting Information S1; Cochran et al., 2009).

The approach we employ in this section assumes that the across-fault velocity contribution along the ray path between the source and the receiver is representative of the velocity heterogeneity vertically below the shallow velocity profile. This is a reasonable assumption in the shallow crust, where ray paths are nearly vertical, but is less applicable at deeper depths. The velocity correction used to account for travel-time differences due to topography is an approximation. Though we cannot perfectly account for elevation, this correction is sufficient for our purposes, because in this section, we are mostly interested in the low velocity zone in our model. This feature is spatially compact and in a segment of the profile with a low topographic gradient. Additionally, the residual profile will be sensitive to contributions along ray paths that are distinct from those of a 1D model, due to 3D effects. We consider these effects by running the sensitivity tests, which incorporate 3D contributions to ray paths for different structural scenarios.

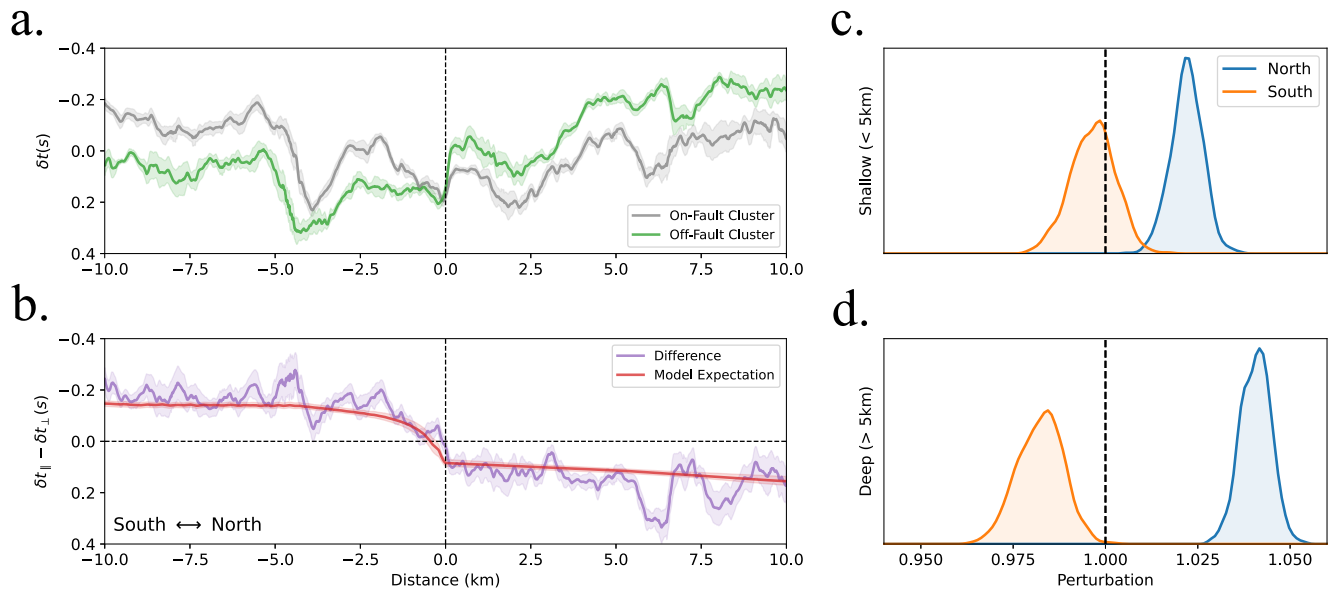


Figure 4. Cluster comparison and inversion results from differential travel-time measurements computed along the yellow segment in Figure 1. (a) Travel-time perturbations from on-fault (gray) and off-fault (green) clusters of earthquakes, shown in Figure 1. (b) Difference between the two sets of perturbations (purple) plotted against the model fit from the inversion ensembles. (c, d) Ensemble results using differential travel-times to invert for the necessary travel-time adjustments for the shallow (c) and deep (d) earth structure to the north and south of the fault. Joint distributions are shown in Figure 5.

The reason for the absence of evidence for a low velocity zone at depth is unclear. If we consider the scaling of fault zone thickness with displacement (Savage & Brodsky, 2011) and the inferred cumulative displacement of approximately 50 km on the Garlock Fault (Davis & Burchfiel, 1973; Monastero et al., 1997; Smith, 1962), we may expect the Garlock Fault damage zone to be hundreds of meters thick at depth. One potential explanation is that we are by chance sampling a segment of the Garlock Fault with narrow damage because of along-strike variability in damage zone thickness due to lithological or geometrical changes (Lin & Yamashita, 2013). Such along-strike variability has been clearly observed both in regional tomographic models and systematic fault zone trapped wave studies (Lewis & Ben-Zion, 2010; Zigone et al., 2015). Given that Q. Qiu et al. (2020) observed no compliant zone deformation in response to the Ridgecrest earthquake over an extensive region, we consider this hypothesis unlikely. Another potential explanation is that the Garlock Fault is simply on the low end of damage zone widths for mature faults. Fault damage zones can have a large variety of widths. For example, the Hector Mine and Landers Faults exhibit widths of approximately 100 m (Y.G. Li, 2002) and 250 m (H. Li et al., 2007; Y. Li et al., 2000) respectively. There is similar variability among mature faults; the Parkfield segment of the San Andreas Fault, which is far more active and mature than the Garlock Fault, hosts a relatively narrow damage zone between 200 and 250 m at depth (Hickman et al., 2007; Y.G. Li et al., 2004). By contrast, the Calico and Anninghe Fault Zones, both late in their interseismic periods, host low velocity zones that in some places exceed widths of 1 km (Cochran et al., 2009; Mu et al., 2024). Mu et al. (2024) partially attribute the wide low velocity zone found at the Anninghe Fault to fault-associated sedimentation. This suggests that factors other than fault damage, such as local geology, may be attributable to the variability in low velocity zone width.

An alternative explanation for the spatially confined damage zone at the Garlock Fault is that considerable fault damage zone healing has potentially taken place over a large segment of the fault, allowing for significant recovery of the seismic velocities in our sensitivity range. This observation is consistent with the absence of fault zone trapped waves near the fault (H. Qiu et al., 2023) and the lack of compliant zone deformation around the fault following the Ridgecrest Earthquake (Q. Qiu et al., 2020). The combination of these factors and the limit on the width of the low velocity zone determined in this study distinguishes the Garlock from the other fault zones mentioned. Because of these complimentary forms of evidence, we favor the hypothesis that the Garlock's damage zone has undergone substantial healing. This possibility has important implications, but it is difficult to verify without knowing the state of the low velocity zone at the beginning of the interseismic period.

4. A Hidden Bimaterial Contrast at Seismogenic Depth

At a broader scale, as shown in Figure 4 and Figure S7 in Supporting Information S1, there is significant variability in the earthquake travel-time perturbations that is not captured by the shallow model. The consequences of this variability depend on whether it is localized above the seismogenic zone or present at seismogenic depths. To help resolve this question, we consider the differential travel-time perturbations between earthquakes. This is based on the observation that earthquakes of variant geographic location have distinct ray paths at depth, but that the ray paths become more similar as they approach the surface. This means that differential perturbations emphasize contributions from deeper depths. We first take the differential perturbations between the cluster of earthquakes on the fault and a different cluster farther to the north. Earthquake waveforms from these clusters are shown in Figure 1 and Figure S8 in Supporting Information S1. The differential perturbation profile shows a consistent difference between perturbation profiles that changes polarity at the fault (Figure 4). Since the earthquakes to the north preferentially sample the northern side of the fault at depth, this differential travel-time profile suggests that the southern side of the fault is faster at depth. Importantly, because of the density of the array and the sharpness of this polarity change, this observation localizes the contrast to the fault. This distinguishes this study from lower resolution tomography models, for which it is not possible to determine whether a velocity contrast is due to a fault or broader structural heterogeneity.

We quantify this observation with a Bayesian inversion using many of the M2+ earthquakes observed by the DAS array. The data in this inversion are the differential travel-time perturbations between every pair of earthquakes, and we solve for the necessary changes in computed travel-times in a simple model below the DAS array to match the data. We compute travel-time perturbations for all M2+ events within 30 km of the intersection between the array and the fault. For this analysis, we consider observations from a 20 km segment of the array centered on the Garlock Fault (yellow curve in Figure 1). We remove any events with mean deviations that are greater than 0.2 s to ensure that we keep events with reliable hypocentral locations, and we subsequently compute the differential travel-time perturbations for each pair of remaining events. The events used in this analysis are plotted in Figure 1 and the depths for these events are given in Figure S9 in Supporting Information S1. Since we are considering interevent travel-time differences recorded by the same channels, these measurements remove the contribution of receiver-side topography. To improve the quality of our data and obtain good estimates of the uncertainty on these measurements, we take the average and standard deviations, which are used as our uncertainties, of these perturbations within 1 km bins. These measurements constitute our data vector. We additionally incorporate the standard deviation of the expected arrival time difference to our error estimates. Since the differential travel-times between the two clusters, and in general those between all event pairs used in this analysis, are simple and the polarity change is sharp and close to the fault, we parameterize a simple 4-block earth structure to resolve the velocity contrast across the fault. The lateral and vertical interfaces between blocks are the Garlock Fault and an approximation of the top of the seismogenic zone (5 km depth below sea level) respectively. We assume the Garlock Fault is vertical based on the fault zone reflected wave observation in Qiu et al. (2023). We formulate our inversion using the equation

$$d_{A_n-B_n} = \sum_i x_i (t_{Ani} - t_{Bni}) - (t_{A_n} - t_{B_n})$$

where t_{Ani} and t_{Bni} are the expected travel-times of events A and B through block i in the model at station n , t_{A_n} and t_{B_n} are the expected total travel-times for events A and B at station n , and x_i is the necessary perturbation to the travel-times through block i to fit the data. The parameters x_i constitute our model vector. An important assumption of this analysis is that the bimaterial contrast does not significantly change between the earthquakes and the array. We also assume the effects of within-fault and broad-scale anisotropy are second order, as we are using a single component measurement and the across fault perturbation change is abrupt.

We apply a simple MCMC approach to solve this inverse problem because of the flexibility of the Bayesian framework and to evaluate tradeoffs between parameters in the inversion. We set a weak Gaussian prior at 1.0 with a standard deviation of 0.1 on each value of x_i to ensure that any perturbation is data informed. As shown in Figure 4, we find that to fit the differential travel-time perturbation profiles, the southern side of the fault is required to be 4%–7% faster than the northern side at seismogenic depths (>5 km). The joint distributions, shown in Figure 5, suggest a narrower distribution of relative values, with a bimaterial contrast at depth well-constrained around 6%. This model matches our data, which requires an abrupt change in differential travel-time at the fault,

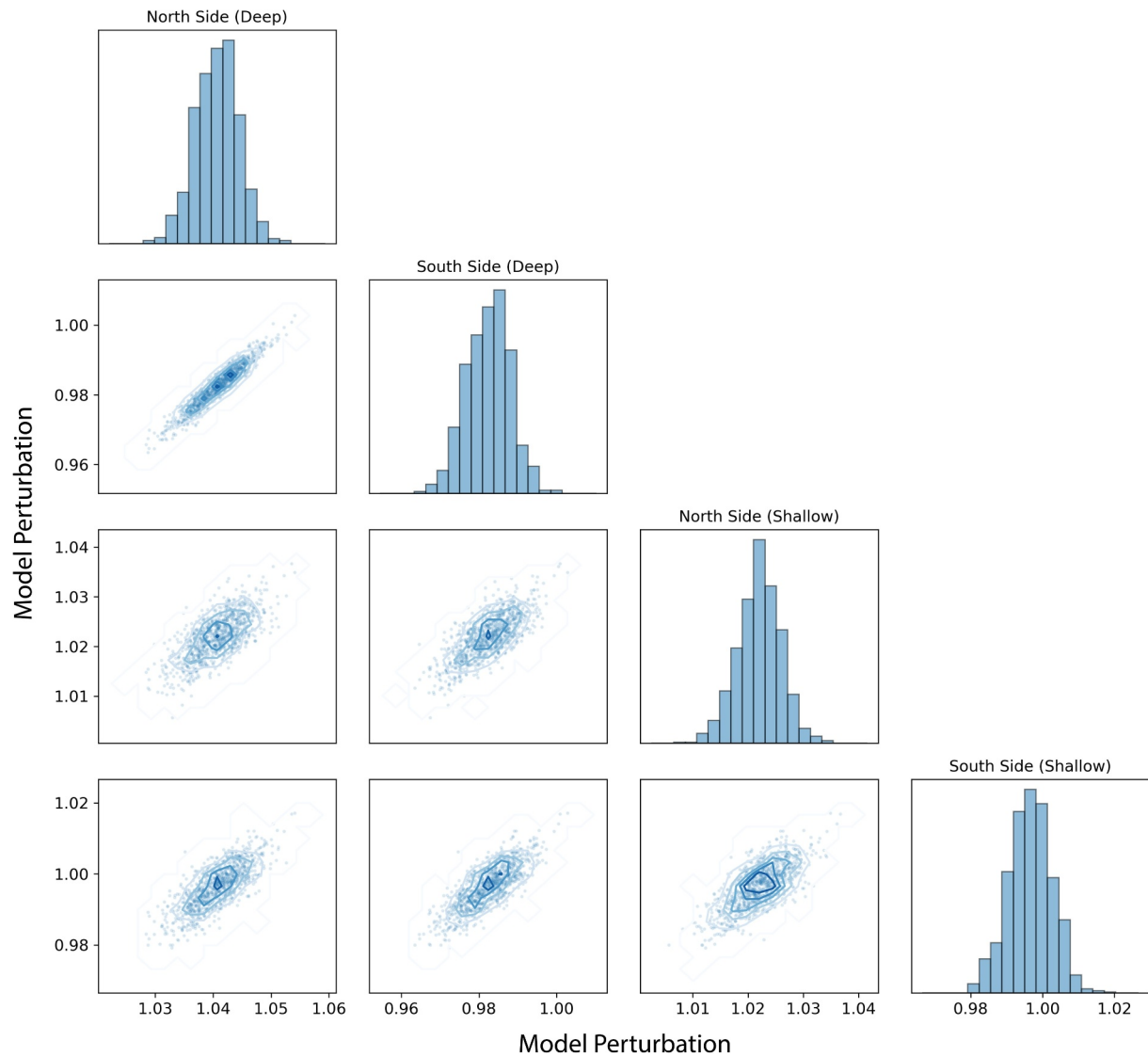


Figure 5. Joint probability distributions for ensembles of parameters from the differential travel-time inversion. Diagonal plots show the marginal distributions (also shown in Figure 4), and the off-diagonal plots show the joint distribution for the row-column pairs. The values in these plots are unitless and correspond to the ratio between the time spent in each quadrant necessary to fit the arrival time data and the expected travel-time spent in each region computed using the initial velocity model.

as shown in Figure 4. This velocity contrast is not apparent in the total travel-time measurements around the fault and was instead hidden by shallow crustal structure, which was largely removed by considering the differential times. Since the expected directivity from bimaterial contrasts corresponds to the sense of slip on the slow side of the fault, this would suggest an increased likelihood that future ruptures have a preferred rupture directivity toward Los Angeles and the San Andreas Fault.

Our measurements are consistent with the CVMS model locally at the array, as shown in Figure S10 in Supporting Information S1, and are also consistent with the tomography model of Tong et al. (2021), who find a similar velocity contrast across the central Garlock fault that reverses polarity at depth. But regional velocity models (E. Lee et al., 2014; White et al., 2021) do not yield a clear picture of a broader velocity contrast along strike. We can corroborate our observation by comparing these results to estimates of velocity profiles from cross-correlations between broadband stations. We consider a year of continuous vertical data on four Southern California Seismic Network broadband stations shown in Figure 6. In a methodology like that described in Section 2, we filter the data between 2 and 100 s and decompose the data into day-long segments. We subsequently perform absolute-average temporal normalization and spectral whitening and cross-correlate the waveforms in the frequency

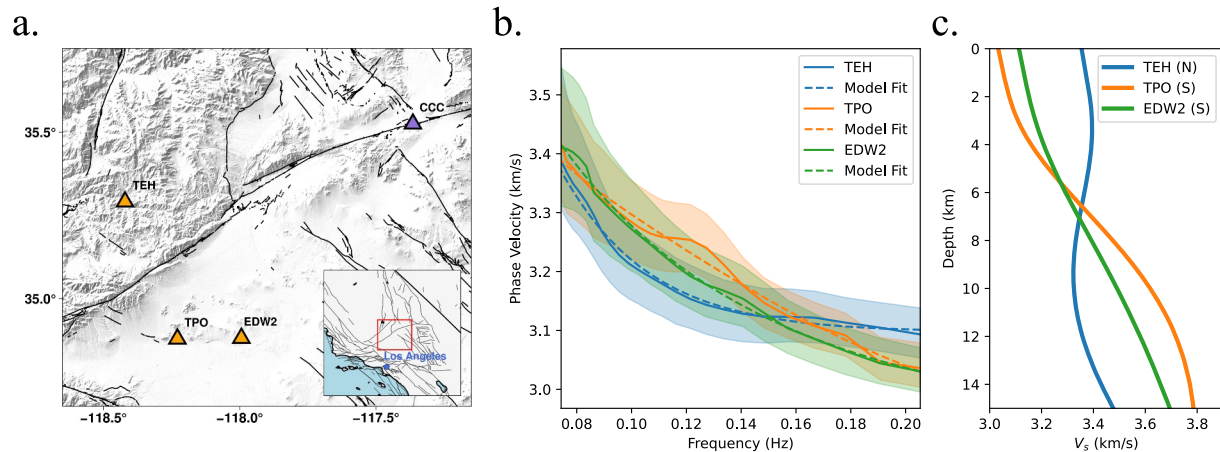


Figure 6. Results from the broadband seismic analysis. (a) Station map showing the stations used in this analysis. Each off-fault station (orange) was cross-correlated with the on-fault station (purple) to produce the corresponding models. (b) The dispersion curves from each of the cross-correlation measurements and (c) the corresponding inverted shear wave velocity profiles.

domain. We then stack the correlograms and consider only the period band between 5 and 13.5 s for this analysis; these frequencies have high sensitivity to the seismogenic zone (approximately 5–15 km) and depths directly above the seismogenic zone. Periods below 5 s did not achieve good convergence and periods above 13.5 s showed substantial phase interference.

We compute the phase dispersion curves by narrowband filtering the data at a set of frequencies and, for each frequency, combine the phase-amplitude relationship with the distance between stations to produce a frequency-velocity dispersion curve. These raw dispersion relationships are shown in Figure S11 in Supporting Information S1. We resolve the 2π ambiguity by picking the frequency-velocity relationship most closely aligned with the Preliminary Reference Earth Model (Dziewonski & Anderson, 1981). We estimate the uncertainty on these measurements using the width of the peak that we pick. We then use surf96 from the Computer Programs in Seismology package (Herrmann, 2013), which applies an iterative, weighted inversion, to recover the 1D shear wave velocity structure from these dispersion curves. The dispersion curves and corresponding velocity profiles are shown in Figure 6. These profiles suggest that in a ~ 100 km window along-strike, encompassing our array, the velocities to the north of the fault are faster at shallow depths but slower below ~ 6 km, which is highly consistent with our local model. The amplitude of the velocity contrast across the fault at depth is also consistent with our local model. This suggests that what we observe in this study is perhaps an extensive rather than a local feature.

5. Discussion and Conclusions

This study provides the depth-localized structure of a major fault zone in California through careful comparisons of multiple forms of analyses with collocated, high spatial density measurements. The deconvolution of measurement contributions from different parts of the fault zone suggests the fault zone model in Figure 7. In particular, the near-surface component of the schematic is determined using the shallow velocity model that incorporates active source and ambient noise phase velocity measurements. The portion of the model at seismogenic depths is determined using the inversion of the differential travel-time perturbation measurements shown in Figure 4. The shallow crust portion of the model is subsequently determined by measuring the residual between the measured travel-times of the cluster of earthquakes on the fault and the expected combined contributions from the near-surface and seismogenic depths. A summary of the travel-time contributions informing this schematic is shown in Figure S7 in Supporting Information S1. Deconvolving the different contributions to depth-integrated measurements is important because depth-integrated measurements may sometimes be misleading. For example, interpreting the fault zone structure using only the depth-integrated travel-time measurements near the fault zone may lead to the conclusion that the low velocity zone to the south of the fault is consistent with a typical persistent fault damage zone structure, and that seismic velocities are faster to the north and slower to the south at seismogenic depths, but these are the opposite conclusions of those presented in this study. These observations likely explain the differences between this study and that of H. Qiu et al. (2023), who

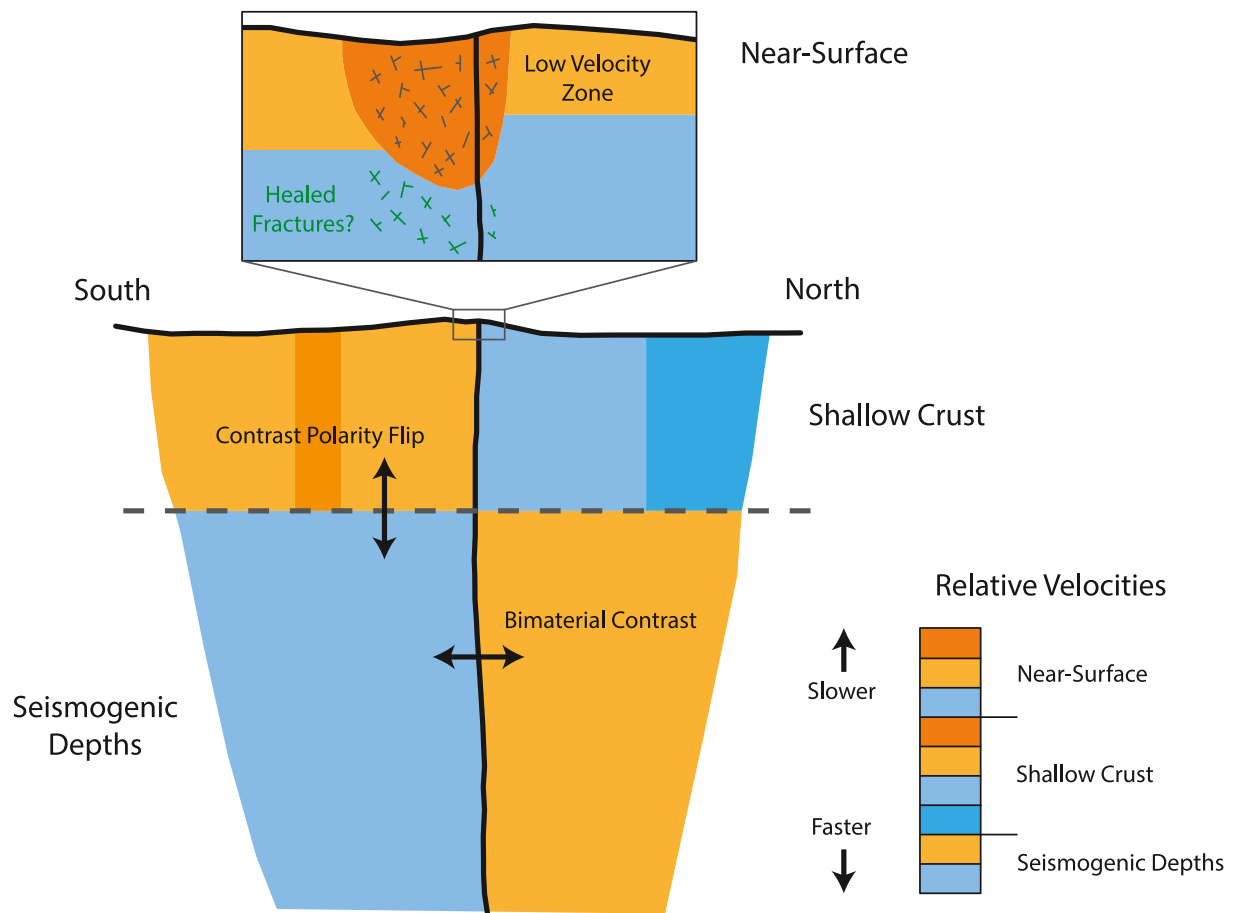


Figure 7. Schematic model summarizing the findings of this study.

used fault zone head waves to determine that the north side of the fault is faster than the south side of the fault. These head wave observations, which are depth-integrated, may have been dominated by the velocity contrast in the shallow crust that is evidenced in Figure S7 in Supporting Information S1 and Figure 6 and illustrated in Figure 7, rather than the contrast with the opposite polarity at seismogenic depth.

These results also show several strengths of DAS for making detailed observations of fault zones. The combined high spatial density of the channels and the low-effort maintenance allowing for long term deployments provide the tools necessary to both perform detailed imaging studies and make observations of many earthquakes with the same array. Performing these analyses with the same array allows for the direct comparison of the results and the subsequent localization of contributions to measurements from depth-localized structures in the fault zone. The application of DAS to fault zone related problems is not limited to the analyses performed in this study, and one can easily envision new possibilities for fault zone research that leverage the strengths of DAS data. For example, DAS arrays deployed across faults could potentially act as long-term, low-maintenance fault zone observatories that could be used to illuminate time-dependent changes in fault zones due to processes such as healing and to better capture seismicity along the fault.

The recovery of seismic velocities in the interseismic period is typically attributed to fault zone healing resulting from fracture closure due to mechanical (Brantley, 1992; Brantley et al., 1990; Brantut et al., 2013) and chemical (Aben et al., 2017; Lee & Morse, 1999; Renard et al., 2000) processes. Studies on fault zones immediately following earthquakes have shown measurable increases in seismic velocity and decreases in permeability with time, suggesting significant healing can take place shortly after an earthquake (Y. G. Li & Vidale, 2001; Marone et al., 1995; Xue et al., 2013). The amount and rate of healing that takes place over the course of the interseismic period is likely highly variable. The presence of low velocity zones and fault zone trapped waves in faults that have not ruptured for decades suggest that some damage zones persist throughout the interseismic period (e.g., Cochran et al., 2009).

Some studies suggest crack healing can occur rapidly, on the order of years (Hiramatsu et al., 2005), and others have observed substantial healing due to the sealing of fractures in exhumed fault zones (Rempe et al., 2018). A recent study using a borehole from the Alpine Fault, another fault late in its interseismic period, suggested that, for at least part of the fault zone, fractures near the fault had little impact on seismic velocity because of extensive mineral precipitation in the fractures (Williams et al., 2016). We speculate that the segment of the Garlock Fault, which is in a region of high hydrothermal activity (Sass et al., 1978), may have experienced similar healing as illustrated in Figure 7. This is evidenced, not only by the low upper limit of damage zone width and velocity perturbation amplitude determined in this study, which is not sufficient evidence by itself, but also by the absence of damage zone indicators such as fault zone trapped waves (H. Qiu et al., 2023) and compliant zone deformation following the Ridgecrest earthquake (Q. Qiu et al., 2020). We cannot definitively say whether this is the case, as the initial state of the damage zone following the last major earthquake is unknown. However, the enigmatic condition of the Garlock Fault's damage zone at depth warrants future study. One potential avenue for future research on this issue would be to investigate borehole data for evidence of healing as done in Williams et al. (2016).

Experimental and observational work investigating the relationship between bimaterial contrasts on faults and rupture directivity have discovered a range of behaviors (e.g., Harris & Day, 2005; Kane et al., 2013; Rubin & Gillard, 2000; Shlomai & Fineberg, 2016; E. Wang & Rubin, 2011; Xia et al., 2005). Dynamic simulations of sequences of ruptures on bimaterial interfaces suggest that, although a material contrast across a fault does not dictate the direction of rupture asymmetry invariably, the presence of a bimaterial contrast over an earthquake sequence creates favorable nucleation sites and increases the likelihood of asymmetric rupture in one direction over the other (Abdelmeguid & Elbanna, 2022; Erickson & Day, 2016). Further complications arise when fault complexity, such as fault curvature and along strike stress variability, is introduced. But, keeping these complications in mind, we can use the observed bimaterial contrast on the Garlock Fault to infer if there is an increased likelihood of a rupture propagating one direction over the other. The Garlock fault perhaps presents an ideal setting for this kind of analysis, as the highly limited low-compliance zone at depth suggests a potentially simpler fault structure. In the case of this study, the bimaterial contrast, which we have localized to seismogenic depths, suggests a future rupture on the Garlock Fault is more likely to propagate toward the San Andreas. This would suggest an increased likelihood of forward directivity ground motion amplitudes to the west of a given rupture, which is an important consideration for both the communities on the fault and those to the west, including Los Angeles. This would also greatly increase the dynamic stress change induced on the San Andreas, and thus may increase the likelihood of a rupture on the Garlock triggering a rupture on the San Andreas (Hill & Prejean, 2015; Toda & Stein, 2020).

Data Availability Statement

The virtual and active source shot gathers used to produce the model shown in Figure 3 and the earthquake data used to produce the profiles shown in Figures 3 and 4 are available at (Atterholt, 2023). The broadband data used to construct the velocity profiles shown in Figure 6 were obtained from the Southern California Seismic Network (SCEDC, 2013). The program used to compute the travel-times for the parametric evaluation of damage zone property sensitivity, Pykonal (White et al., 2020). Ray paths for the inversion of the velocity contrast across the fault were computed using the TauP (Crotwell et al., 1999) functionality in Obspy (Krischer et al., 2015). Figure 1 was made using The Generic Mapping Tools (GMT), version 6 (Wessel et al., 2019).

References

- Abdelmeguid, M., & Elbanna, A. (2022). Sequences of seismic and aseismic slip on bimaterial faults show dominant rupture asymmetry and potential for elevated seismic hazard. *Earth and Planetary Science Letters*, 593, 117648. <https://doi.org/10.1016/j.epsl.2022.117648>
- Aben, F. M., Doan, M.-L., Gratier, J.-P., & Renard, F. (2017). Experimental postseismic recovery of fractured rocks assisted by calcite sealing: Experimental recovery of fractured rocks. *Geophysical Research Letters*, 44(14), 7228–7238. <https://doi.org/10.1002/2017GL073965>
- Aki, K. (1993). Local site effects on weak and strong ground motion. *Tectonophysics*, 218(1–3), 93–111. [https://doi.org/10.1016/0040-1951\(93\)90262-i](https://doi.org/10.1016/0040-1951(93)90262-i)
- Allam, A. A., Ben-Zion, Y., & Peng, Z. (2014). Seismic imaging of a bimaterial interface along the Hayward Fault, CA, with fault zone head waves and direct P arrivals. *Pure and Applied Geophysics*, 171(11), 2993–3011. <https://doi.org/10.1007/s00024-014-0784-0>
- Andrews, D. J., & Ben-Zion, Y. (1997). Wrinkle-like slip pulse on a fault between different materials. *Journal of Geophysical Research*, 102(B1), 553–571. <https://doi.org/10.1029/96JB02856>
- Anooshehpour, A., & Brune, J. N. (1999). Wrinkle-like Weertman pulse at the interface between two blocks of foam rubber with different velocities. *Geophysical Research Letters*, 26(13), 2025–2028. <https://doi.org/10.1029/1999GL900397>
- Atterholt, J. (2023). Garlock DAS dataset [Dataset]. *Caltech DATA*. <https://doi.org/10.22002/923s-4p068>

Acknowledgments

We would like to thank Dr. Robert Clayton and Dr. Martin Karrenbach for their help in performing the active source survey. We would also like to thank Dr. John Vidale, Dr. Elizabeth Cochran, Dr. Hongrui Qiu, Dr. Heather Savage, Dr. Yihe Huang, Dr. Ahmed Elbanna, and Dr. Ares Rosakis for their insightful conversations and suggestions which greatly improved the paper. James Atterholt was supported by the National Science Foundation (NSF) Graduate Research Fellowship Program (GRFP) number DGE-1745301. The study was made possible by the Gordon Moore Foundation and the National Science Foundation (NSF) through the Faculty Early Career Development (CAREER) award number 1848166. We would also like to thank the California Broadband Cooperative for allowing access to the fiber used for the DAS array in this experiment. Finally, we would like to thank the editor Dr. Fenglin Niu for facilitating the review process and two anonymous reviewers for their suggestions.

- Atterholt, J., & Ross, Z. E. (2023). Finite source properties of large strike-slip earthquakes. *Geophysical Journal International*, 236(2), ggad459. <https://doi.org/10.1093/gji/ggad459>
- Atterholt, J., Zhan, Z., & Yang, Y. (2022). Fault zone imaging with distributed acoustic sensing: Body-to-surface wave scattering. *Journal of Geophysical Research: Solid Earth*, 127(11), e2022JB025052. <https://doi.org/10.1029/2022JB025052>
- Bensen, G. D., Ritzwoller, M. H., Barmin, M. P., Levshin, A. L., Lin, F., Moschetti, M. P., et al. (2007). Processing seismic ambient noise data to obtain reliable broad-band surface wave dispersion measurements. *Geophysical Journal International*, 169(3), 1239–1260. <https://doi.org/10.1111/j.1365-246X.2007.03374.x>
- Ben-Zion, Y., Peng, Z., Okaya, D., Seeber, L., Armbruster, J. G., Ozer, N., et al. (2003). A shallow fault-zone structure illuminated by trapped waves in the Karadere-Duzce branch of the North Anatolian Fault, western Turkey. *Geophysical Journal International*, 152(3), 699–717. <https://doi.org/10.1046/j.1365-246X.2003.01870.x>
- Brantley, S. L. (1992). The effect of fluid chemistry on quartz microcrack lifetimes. *Earth and Planetary Science Letters*, 113(1–2), 145–156. [https://doi.org/10.1016/0012-821X\(92\)90216-1](https://doi.org/10.1016/0012-821X(92)90216-1)
- Brantley, S. L., Evans, B., Hickman, S. H., & Crerar, D. A. (1990). Healing of microcracks in quartz: Implications for fluid flow. *Geology*, 18(2), 136. [https://doi.org/10.1130/0091-7613\(1990\)018<0136:HOMIQI>2.3.CO;2](https://doi.org/10.1130/0091-7613(1990)018<0136:HOMIQI>2.3.CO;2)
- Brantut, N., Heap, M. J., Meredith, P. G., & Baud, P. (2013). Time-dependent cracking and brittle creep in crustal rocks: A review. *Journal of Structural Geology*, 52, 17–43. <https://doi.org/10.1016/j.jsg.2013.03.007>
- Caine, J. S., Evans, J. P., & Forster, C. B. (1996). Fault zone architecture and permeability structure. *Geology*, 24(11), 1025. [https://doi.org/10.1130/0091-7613\(1996\)024<1025:FZAAPS>2.3.CO;2](https://doi.org/10.1130/0091-7613(1996)024<1025:FZAAPS>2.3.CO;2)
- Catchings, R. D., Goldman, M. R., Li, Y. G., & Chan, J. H. (2016). Continuity of the West Napa–Franklin Fault Zone inferred from guided waves generated by earthquakes following the 24 August 2014 M_w 6.0 South Napa Earthquake. *Bulletin of the Seismological Society of America*, 106(6), 2721–2746. <https://doi.org/10.1785/0120160154>
- Cheng, F., Chi, B., Lindsey, N. J., Dawe, T. C., & Ajo-Franklin, J. B. (2021). Utilizing distributed acoustic sensing and ocean bottom fiber optic cables for submarine structural characterization. *Scientific Reports*, 11(1), 5613. <https://doi.org/10.1038/s41598-021-84845-y>
- Cochard, A., & Rice, J. R. (2000). Fault rupture between dissimilar materials: Ill-posedness, regularization, and slip-pulse response. *Journal of Geophysical Research*, 105(B11), 25891–25907. <https://doi.org/10.1029/2000JB900230>
- Cochran, E. S., Li, Y.-G., Shearer, P. M., Barbot, S., Fialko, Y., & Vidale, J. E. (2009). Seismic and geodetic evidence for extensive, long-lived fault damage zones. *Geology*, 37(4), 315–318. <https://doi.org/10.1130/G25306A.1>
- Crotwell, H. P., Owens, T. J., & Ritsema, J. (1999). The TauP Toolkit: Flexible seismic travel-time and ray-path utilities. *Seismological Research Letters*, 70(2), 154–160. <https://doi.org/10.1785/gssrl.70.2.154>
- Davis, G. A., & Burchfiel, B. C. (1973). Garlock Fault: An intracontinental transform structure, Southern California. *Geological Society of America Bulletin*, 84(4), 1407. [https://doi.org/10.1130/0016-7606\(1973\)84<1407:GFAITS>2.0.CO;2](https://doi.org/10.1130/0016-7606(1973)84<1407:GFAITS>2.0.CO;2)
- Dawson, T. E., McGill, S. F., & Rockwell, T. K. (2003). Irregular recurrence of paleoearthquakes along the central Garlock fault near El Paso Peaks, California: Irregular recurrence of paleoearthquakes. *Journal of Geophysical Research*, 108(B7), 2356. <https://doi.org/10.1029/2001JB001744>
- Dunham, E. M., Belanger, D., Cong, L., & Kozdon, J. E. (2011). Earthquake ruptures with strongly rate-weakening friction and off-fault plasticity, Part I: Planar faults. *Bulletin of the Seismological Society of America*, 101(5), 2296–2307. <https://doi.org/10.1785/0120100075>
- Dziewonski, A. M., & Anderson, D. (1981). Preliminary reference Earth model. *Physics of the Earth and Planetary Interiors*, 25(4), 297–356. [https://doi.org/10.1016/0031-9201\(81\)90046-7](https://doi.org/10.1016/0031-9201(81)90046-7)
- Erickson, B. A., & Day, S. M. (2016). Bimaterial effects in an earthquake cycle model using rate-and-state friction. *Journal of Geophysical Research: Solid Earth*, 121(4), 2480–2506. <https://doi.org/10.1002/2015JB012470>
- Garbuno-Inigo, A., Hoffmann, F., Li, W., & Stuart, A. M. (2020). Interacting Langevin diffusions: Gradient structure and ensemble Kalman sampler. *SIAM Journal on Applied Dynamical Systems*, 19(1), 412–441. <https://doi.org/10.1137/19M1251655>
- Hadley, D., & Kanamori, H. (1977). Seismic structure of the transverse ranges, California. *Geological Society of America Bulletin*, 88(10), 1469. [https://doi.org/10.1130/0016-7606\(1977\)88<1469:SSOTTR>2.0.CO;2](https://doi.org/10.1130/0016-7606(1977)88<1469:SSOTTR>2.0.CO;2)
- Harris, R. A., & Day, S. M. (2005). Material contrast does not predict earthquake rupture propagation direction. *Geophysical Research Letters*, 32(23), L23301. <https://doi.org/10.1029/2005GL023941>
- Hauksson, E., Yang, W., & Shearer, P. M. (2012). Waveform relocated earthquake catalog for Southern California (1981 to June 2011). *Bulletin of the Seismological Society of America*, 102(5), 2239–2244. <https://doi.org/10.1785/0120120010>
- Herrmann, R. B. (2013). Computer programs in seismology: An evolving tool for instruction and research. *Seismological Research Letters*, 84(6), 1081–1088. <https://doi.org/10.1785/0220110096>
- Hickman, S., Zoback, M., Ellsworth, W., Boness, N., Malin, P., Roecker, S., & Thurber, C. (2007). Structure and properties of the San Andreas Fault in Central California: Recent results from the SAFOD experiment. *Scientific Drilling, Special Issue*, 29–32. <https://doi.org/10.5194/sd-SpecialIssue-29-2007>
- Hill, D. P., & Prejean, S. G. (2015). Dynamic triggering. In *Treatise on geophysics* (pp. 273–304). Elsevier. <https://doi.org/10.1016/B978-0-444-53802-4.00078-6>
- Hiramatsu, Y., Honma, H., Saiga, A., Furumoto, M., & Ooida, T. (2005). Seismological evidence on characteristic time of crack healing in the shallow crust. *Geophysical Research Letters*, 32(9), 2005GL022657. <https://doi.org/10.1029/2005GL022657>
- Huang, Y. (2018). Earthquake rupture in fault zones with along-strike material heterogeneity. *Journal of Geophysical Research: Solid Earth*, 123(11), 9884–9898. <https://doi.org/10.1029/2018JB016354>
- Jia, Z., Jin, Z., Marchandon, M., Ulrich, T., Gabriel, A.-A., Fan, W., et al. (2023). The complex dynamics of the 2023 Kahramanmaraş, Turkey, M_w 7.8–7.7 earthquake doublet. *Science*, 381(6661), 985–990. <https://doi.org/10.1126/science.adf0685>
- Jiang, X., Hu, S., & Yang, H. (2021). Depth extent and V_p/V_s ratio of the Chenghai Fault Zone, Yunnan, China constrained from dense-array-based teleseismic receiver functions. *Journal of Geophysical Research: Solid Earth*, 126(8), e2021JB022190. <https://doi.org/10.1029/2021JB022190>
- Jousset, P., Reinsch, T., Ryberg, T., Blanck, H., Clarke, A., Aghayev, R., et al. (2018). Dynamic strain determination using fibre-optic cables allows imaging of seismological and structural features. *Nature Communications*, 9(1), 2509. <https://doi.org/10.1038/s41467-018-04860-y>
- Kane, D. L., Shearer, P. M., Goertz-Allmann, B. P., & Vernon, F. L. (2013). Rupture directivity of small earthquakes at Parkfield. *Journal of Geophysical Research: Solid Earth*, 118(1), 212–221. <https://doi.org/10.1029/2012JB009675>
- Krischer, L., Megies, T., Barsch, R., Beyreuther, M., Lecocq, T., Caudron, C., & Wassermann, J. (2015). ObsPy: A bridge for seismology into the scientific Python ecosystem. *Computational Science & Discovery*, 8(1), 014003. <https://doi.org/10.1088/1749-4699/8/1/014003>

- Lee, E., Chen, P., Jordan, T. H., Maechling, P. B., Denolle, M. A. M., & Beroza, G. C. (2014). Full-3-D tomography for crustal structure in Southern California based on the scattering-integral and the adjoint-wavefield methods. *Journal of Geophysical Research: Solid Earth*, 119(8), 6421–6451. <https://doi.org/10.1002/2014JB011346>
- Lee, Y.-J., & Morse, J. W. (1999). Calcite precipitation in synthetic veins: Implications for the time and fluid volume necessary for vein filling. *Chemical Geology*, 156(1–4), 151–170. [https://doi.org/10.1016/S0009-2541\(98\)00183-1](https://doi.org/10.1016/S0009-2541(98)00183-1)
- Lewis, M. A., & Ben-Zion, Y. (2010). Diversity of fault zone damage and trapping structures in the Parkfield section of the San Andreas Fault from comprehensive analysis of near fault seismograms: Diversity of fault zone damage at Parkfield. *Geophysical Journal International*, 183(3), 1579–1595. <https://doi.org/10.1111/j.1365-246X.2010.04816.x>
- Li, H., Zhu, L., & Yang, H. (2007). High-resolution structures of the Landers fault zone inferred from aftershock waveform data: High-resolution Landers fault zone structures. *Geophysical Journal International*, 171(3), 1295–1307. <https://doi.org/10.1111/j.1365-246X.2007.03608.x>
- Li, Y., Vidale, J. E., Aki, K., & Xu, F. (2000). Depth-dependent structure of the Landers fault zone from trapped waves generated by aftershocks. *Journal of Geophysical Research*, 105(B3), 6237–6254. <https://doi.org/10.1029/1999JB900449>
- Li, Y.-G. (2002). Study of the 1999 M 7.1 Hector Mine, California, earthquake Fault Plane by trapped waves. *Bulletin of the Seismological Society of America*, 92(4), 1318–1332. <https://doi.org/10.1785/0120000909>
- Li, Y.-G., & Vidale, J. E. (2001). Healing of the shallow fault zone from 1994–1998 after the 1992 M 7.5 Landers, California, Earthquake. *Geophysical Research Letters*, 28(15), 2999–3002. <https://doi.org/10.1029/2001GL012922>
- Li, Y.-G., Vidale, J. E., & Cochran, E. S. (2004). Low-velocity damaged structure of the San Andreas Fault at Parkfield from fault zone trapped waves: Low-velocity damaged structure of the San Andreas Fault. *Geophysical Research Letters*, 31(12), L12S06. <https://doi.org/10.1029/2003GL019044>
- Lin, A., & Yamashita, K. (2013). Spatial variations in damage zone width along strike-slip faults: An example from active faults in southwest Japan. *Journal of Structural Geology*, 57, 1–15. <https://doi.org/10.1016/j.jsg.2013.10.006>
- Madden Madugo, C., Dolan, J. F., & Hartleb, R. D. (2012). New Paleoearthquake Ages from the Western Garlock Fault: Implications for regional earthquake occurrence in Southern California. *Bulletin of the Seismological Society of America*, 102(6), 2282–2299. <https://doi.org/10.1785/0120110310>
- Marone, C., Vidale, J. E., & Ellsworth, W. L. (1995). Fault healing inferred from time dependent variations in source properties of repeating earthquakes. *Geophysical Research Letters*, 22(22), 3095–3098. <https://doi.org/10.1029/95GL03076>
- McGill, S., & Rockwell, T. (1998). Ages of Late Holocene earthquakes on the central Garlock fault near El Paso Peaks, California. *Journal of Geophysical Research*, 103(B4), 7265–7279. <https://doi.org/10.1029/97JB02129>
- McGuire, J., & Ben-Zion, Y. (2005). High-resolution imaging of the Bear Valley section of the San Andreas fault at seismogenic depths with fault-zone head waves and relocated seismicity. *Geophysical Journal International*, 163(1), 152–164. <https://doi.org/10.1111/j.1365-246X.2005.02703.x>
- McGuire, J. J., Zhao, L., & Jordan, T. H. (2002). Predominance of unilateral rupture for a global catalog of large earthquakes. *Bulletin of the Seismological Society of America*, 92(8), 3309–3317. <https://doi.org/10.1785/0120010293>
- Monastero, F. C., Sabin, A. E., & Walker, J. D. (1997). Evidence for post-early Miocene initiation of movement on the Garlock fault from offset of the Cudahy Camp Formation, east-central California. *Geology*, 25(3), 247. [https://doi.org/10.1130/0091-7613\(1997\)025<0247:EFPEMI>2.3.CO;2](https://doi.org/10.1130/0091-7613(1997)025<0247:EFPEMI>2.3.CO;2)
- Mu, X., Song, J., Yang, H., Huang, J., Yao, H., & Tian, B. (2024). High-resolution shallow structure along the Anninghe Fault Zone, Sichuan, China, constrained by active source tomography. *Seismological Research Letters*, 95(1), 408–420. <https://doi.org/10.1785/0220230137>
- Muir, J. B., Clayton, R. W., Tsai, V. C., & Brissaud, Q. (2022). Parsimonious velocity inversion applied to the Los Angeles Basin, CA. *Journal of Geophysical Research: Solid Earth*, 127(2), e2021JB023103. <https://doi.org/10.1029/2021JB023103>
- Muir, J. B., & Tsai, V. C. (2020). Geometric and level set tomography using ensemble Kalman inversion. *Geophysical Journal International*, 220(2), 967–980. <https://doi.org/10.1093/gji/ggz472>
- Ozakin, Y., Ben-Zion, Y., Aktar, M., Karabulut, H., & Peng, Z. (2012). Velocity contrast across the 1944 rupture zone of the North Anatolian fault east of Ismetpasa from analysis of teleseismic arrivals: Velocity contrast on NAF from teleseisms. *Geophysical Research Letters*, 39(8), L08307. <https://doi.org/10.1029/2012GL051426>
- Qiu, H., Chi, B., & Ben-Zion, Y. (2023). Internal structure of the Central Garlock Fault Zone from Ridgecrest aftershocks recorded by dense linear seismic arrays. *Geophysical Research Letters*, 50(2), e2022GL101761. <https://doi.org/10.1029/2022GL101761>
- Qiu, H., Niu, F., & Qin, L. (2021). Denoising surface waves extracted from ambient noise recorded by 1-D linear array using three-station interferometry of direct waves. *Journal of Geophysical Research: Solid Earth*, 126(8), e2021JB021712. <https://doi.org/10.1029/2021JB021712>
- Qiu, Q., Barbot, S., Wang, T., & Wei, S. (2020). Slip complementarity and triggering between the foreshock, mainshock, and afterslip of the 2019 ridgecrest rupture sequence. *Bulletin of the Seismological Society of America*, 110(4), 1701–1715. <https://doi.org/10.1785/0120200037>
- Ranjith, K., & Rice, J. (2001). Slip dynamics at an interface between dissimilar materials. *Journal of the Mechanics and Physics of Solids*, 49(2), 341–361. [https://doi.org/10.1016/S0022-5096\(00\)00029-6](https://doi.org/10.1016/S0022-5096(00)00029-6)
- Rempe, M., Mitchell, T. M., Renner, J., Smith, S. A. F., Bistacchi, A., & Di Toro, G. (2018). The relationship between microfracture damage and the physical properties of fault-related rocks: The Gole Larghe Fault Zone, Italian Southern Alps. *Journal of Geophysical Research: Solid Earth*, 123(9), 7661–7687. <https://doi.org/10.1029/2018JB015900>
- Renard, F., Gratier, J.-P., & Jamtveit, B. (2000). Kinetics of crack-sealing, intergranular pressure solution, and compaction around active faults. *Journal of Structural Geology*, 22(10), 1395–1407. [https://doi.org/10.1016/S0191-8141\(00\)00064-X](https://doi.org/10.1016/S0191-8141(00)00064-X)
- Ross, Z. E., Idini, B., Jia, Z., Stephenson, O. L., Zhong, M., Wang, X., et al. (2019). Hierarchical interlocked orthogonal faulting in the 2019 Ridgecrest earthquake sequence. *Science*, 366(6463), 346–351. <https://doi.org/10.1126/science.aaz0109>
- Rubin, A. M., & Gillard, D. (2000). Aftershock asymmetry/rupture directivity among central San Andreas fault microearthquakes. *Journal of Geophysical Research*, 105(B8), 19095–19109. <https://doi.org/10.1029/2000JB900129>
- Sass, J., Galanis, S., Marshall, B., Lachenbruch, A., Munroe, R., & Moses, T. (1978). *Conductive heat flow in the Randsburg area*. University of North Texas Libraries. Retrieved from <https://digital.library.unt.edu/ark:/67531/metadc1108190/m1/9/>
- Savage, H. M., & Brodsky, E. E. (2011). Collateral damage: Evolution with displacement of fracture distribution and secondary fault strands in fault damage zones. *Journal of Geophysical Research*, 116(B3), B03405. <https://doi.org/10.1029/2010JB007665>
- SCEDC. (2013). Southern California earthquake center [Dataset]. *SCEDC*. <https://doi.org/10.7909/C3WD3xH1>
- Sethian, J. A. (1996). A fast marching level set method for monotonically advancing fronts. *Proceedings of the National Academy of Sciences*, 93(4), 1591–1595. <https://doi.org/10.1073/pnas.93.4.1591>
- Share, P.-E., Tábořík, P., Štěpánčíková, P., Stemberk, J., Rockwell, T. K., Wade, A., et al. (2020). Characterizing the uppermost 100 m structure of the San Jacinto fault zone southeast of Anza, California, through joint analysis of geological, topographic, seismic and resistivity data. *Geophysical Journal International*, 222(2), 781–794. <https://doi.org/10.1093/gji/ggaa204>

- Shlomai, H., & Fineberg, J. (2016). The structure of slip-pulses and supershear ruptures driving slip in bimaterial friction. *Nature Communications*, 7(1), 11787. <https://doi.org/10.1038/ncomms11787>
- Smith, G. (1962). Large lateral displacement on Garlock Fault, California, as measured from offset dike swarm. *AAPG Bulletin*, 46. <https://doi.org/10.1306/BC74375F-16BE-11D7-8645000102C1865D>
- Song, J., & Yang, H. (2022). Seismic site response inferred from records at a dense linear array across the Chenghai Fault Zone, Binchuan, Yunnan. *Journal of Geophysical Research: Solid Earth*, 127(1). <https://doi.org/10.1029/2021JB022710>
- Spica, Z. J., Perton, M., Martin, E. R., Beroza, G. C., & Biondi, B. (2020). Urban seismic site characterization by fiber-optic seismology. *Journal of Geophysical Research: Solid Earth*, 125(3), e2019JB018656. <https://doi.org/10.1029/2019JB018656>
- Thakur, P., Huang, Y., & Kaneko, Y. (2020). Effects of low-velocity Fault Damage Zones on long-term earthquake behaviors on mature strike-slip faults. *Journal of Geophysical Research: Solid Earth*, 125(8). <https://doi.org/10.1029/2020JB019587>
- Toda, S., & Stein, R. S. (2020). Long- and short-term stress interaction of the 2019 Ridgecrest sequence and coulomb-based earthquake forecasts. *Bulletin of the Seismological Society of America*, 110(4), 1765–1780. <https://doi.org/10.1785/0120200169>
- Tong, P., Yao, J., Liu, Q., Li, T., Wang, K., Liu, S., et al. (2021). Crustal rotation and fluids: Factors for the 2019 Ridgecrest earthquake sequence? *Geophysical Research Letters*, 48(3), e2020GL090853. <https://doi.org/10.1029/2020GL090853>
- Viens, L., Perton, M., Spica, Z. J., Nishida, K., Yamada, T., & Shinohara, M. (2022). Understanding surface wave modal content for high-resolution imaging of submarine sediments with distributed acoustic sensing. *Geophysical Journal International*, 232(3), 1668–1683. <https://doi.org/10.1093/gji/ggac420>
- Wang, E., & Rubin, A. M. (2011). Rupture directivity of microearthquakes on the San Andreas Fault from spectral ratio inversion: Bimaterial microearthquake directivity. *Geophysical Journal International*, 186(2), 852–866. <https://doi.org/10.1111/j.1365-246X.2011.05087.x>
- Wang, Y., Allam, A., & Lin, F. (2019). Imaging the Fault Damage Zone of the San Jacinto Fault Near Anza with ambient noise tomography using a dense nodal array. *Geophysical Research Letters*, 46(22), 12938–12948. <https://doi.org/10.1029/2019GL084835>
- Wessel, P., Luis, J., Uieda, L., Scharroo, R., Wobbe, F., Smith, W., & Tian, D. (2019). The generic mapping tools [Computer software]. *Generic-Mapping-Tools*. <https://www.generic-mapping-tools.org/>
- White, M. C. A., Fang, H., Catchings, R. D., Goldman, M. R., Steidl, J. H., & Ben-Zion, Y. (2021). Detailed traveltimes tomography and seismic catalogue around the 2019 M 7.1 Ridgecrest, California, earthquake using dense rapid-response seismic data. *Geophysical Journal International*, 227(1), 204–227. <https://doi.org/10.1093/gji/ggab224>
- White, M. C. A., Fang, H., Nakata, N., & Ben-Zion, Y. (2020). PyKonal: A python package for solving the Eikonal equation in Spherical and Cartesian coordinates using the fast marching method. *Seismological Research Letters*, 91(4), 2378–2389. <https://doi.org/10.1785/0220190318>
- Williams, J. N., Toy, V. G., Massiot, C., McNamara, D. D., & Wang, T. (2016). Damaged beyond repair? Characterising the damage zone of a fault late in its interseismic cycle, the Alpine Fault, New Zealand. *Journal of Structural Geology*, 90, 76–94. <https://doi.org/10.1016/j.jsg.2016.07.006>
- Xia, K., Rosakis, A. J., Kanamori, H., & Rice, J. R. (2005). Laboratory earthquakes along inhomogeneous faults: Directionality and Supershear. *Science*, 308(5722), 681–684. <https://doi.org/10.1126/science.1108193>
- Xue, L., Li, H.-B., Brodsky, E. E., Xu, Z.-Q., Kano, Y., Wang, H., et al. (2013). Continuous permeability measurements record healing inside the Wenchuan Earthquake Fault Zone. *Science*, 340(6140), 1555–1559. <https://doi.org/10.1126/science.1237237>
- Yang, Y., Atterholt, J. W., Shen, Z., Muir, J. B., Williams, E. F., & Zhan, Z. (2022). Sub-kilometer correlation between near-surface structure and ground motion measured with distributed acoustic sensing. *Geophysical Research Letters*, 49(1), e2021GL096503. <https://doi.org/10.1029/2021GL096503>
- Yang, Y., Zhan, Z., Shen, Z., & Atterholt, J. (2022). Fault Zone imaging with distributed acoustic sensing: Surface-to-surface wave scattering. *Journal of Geophysical Research: Solid Earth*, 127(6), e2022JB024329. <https://doi.org/10.1029/2022JB024329>
- Zhang, Z., Deng, Y., Qiu, H., Peng, Z., & Liu-Zeng, J. (2022). High-resolution imaging of Fault Zone Structure along the creeping section of the Haiyuan Fault, NE Tibet, from data recorded by dense seismic arrays. *Journal of Geophysical Research: Solid Earth*, 127(9), e2022JB024468. <https://doi.org/10.1029/2022JB024468>
- Zhu, W., & Beroza, G. C. (2018). PhaseNet: A deep-neural-network-based seismic arrival time picking method. *Geophysical Journal International*. <https://doi.org/10.1093/gji/ggy423>
- Zhu, W., Biondi, E., Li, J., Yin, J., Ross, Z. E., & Zhan, Z. (2023). Seismic arrival-time picking on distributed acoustic sensing data using semi-supervised learning. *Nature Communications*, 14(1), 8192. <https://doi.org/10.1038/s41467-023-43355-3>
- Zhu, W., McBrearty, I. W., Mousavi, S. M., Ellsworth, W. L., & Beroza, G. C. (2022). Earthquake phase association using a Bayesian Gaussian mixture model. *Journal of Geophysical Research: Solid Earth*, 127(5), e2021JB023249. <https://doi.org/10.1029/2021JB023249>
- Zigone, D., Ben-Zion, Y., Campillo, M., & Roux, P. (2015). Seismic tomography of the Southern California Plate Boundary Region from noise-based Rayleigh and Love Waves. *Pure and Applied Geophysics*, 172(5), 1007–1032. <https://doi.org/10.1007/s00024-014-0872-1>
- Zigone, D., Ben-Zion, Y., Lehujeur, M., Campillo, M., Hillers, G., & Vernon, F. L. (2019). Imaging subsurface structures in the San Jacinto fault zone with high-frequency noise recorded by dense linear arrays. *Geophysical Journal International*, 217(2), 879–893. <https://doi.org/10.1093/gji/ggz069>